Three-Dimensional Microscale Imaging and Measurement of Soft Material Contact Interfaces Under Quasi-Static Normal Indentation and Shear

Karl G. Johannes[*], *Kristin N. Calahan*[*], (*[*]*: equal contributions) Yuan Qi, Rong Long, Mark E. Rentschler*

Department of Mechanical Engineering, University of Colorado, Boulder, Colorado 80309, United States

ABSTRACT (Word Style "BD_Abstract"). Understanding the contact and friction of soft materials is vital for a wide variety of engineering applications including soft sealants and medical devices such as catheters and stents. While the mechanisms of friction between stiff materials have been extensively studied, the mechanisms of friction between soft materials are much less understood. Time dependent material responses, large deformations and fluid layers at the contact interface, common in soft materials, pose new challenges toward understanding friction of soft materials. This paper aims to characterize the three-dimensional (3D) contact interfaces in soft materials under large deformation and complex contact conditions. Specifically, we introduce a micro-indentation and visualization (MIV) system capable of investigating soft material contact interfaces with combined normal and shear loading. When combined with a laser scanning confocal microscope, the MIV system enables the acquisition of 3D image stacks of the deformed

substrate and the indenter, under fixed normal and shear displacements. The 3D imaging data allows us to quantify the 3D contact profiles and correlate them with the applied normal and shear displacements. Using a spherical indenter and a hydrogel substrate as a model system, we demonstrate that the MIV system and the associated analysis techniques accurately measure the contact area under combined normal and shear loading. Although the limited speed of confocal scanning implies that this method is most suitable for quasi-static loading conditions, potential methods to increase the imaging speed and the corresponding trade-off in image resolution are discussed. The method presented here will be useful for future investigation of soft material contact and friction involving complex surface geometries.

Keywords: Three-dimensional interface, indentation, confocal imaging, contact area, friction

Introduction:

Friction between two stiff materials arises from contact and deformation of surface asperities on the contact interface [1,2]. The significant research efforts that led to the current understanding of tribology have been critical to improving the wear and efficiency of many classical engineered systems such as engines and transmissions[3,4]. Soft tribology, on the other hand, is an emerging area that has not been explored to the same depths[5]. Fundamental knowledge of soft tribology underlies many new technological applications such as soft robotics[6], tissue engineering[7], and medical devices[8]. For example, medical robotic devices capable of interfacing with soft tissues in physiological environments (e.g. the gastrointestinal tract) are promising solutions for future autonomous diagnosis and surgical intervention[9]. *In vivo* locomotion of robotic devices would inevitably involve contact and friction with soft tissue, which is not yet well understood. Time-dependent mechanical behaviors (e.g. viscoelasticity and poroelasticity), inherent nonlinearities

due to large deformation, and the presence of a fluid layer on the interface all pose significant challenges towards understanding the mechanics of friction on soft tissue, or more broadly soft materials. More specifically viscoelasticity was found to play an important role in rubber friction by generating energy dissipation associated with rubber deformation[10]. For hydrogels, in addition to viscoelasticity[11], poroelasticity is a key mechanism governing the relaxation upon indentation[12,13] and frictional resistance under steady state sliding[14,15]. Effects of these time-dependent mechanical behaviors on contact and friction are coupled to the deformation in the soft materials, which is often far beyond the linear regime especially for soft tissue or gels[16,17]. Large deformation of soft material upon contact and friction results in nonlinear deformation and stress fields[18] that are difficult to characterize. Recently, it was discovered that lubrication forces due to interfacial fluid layer can cause considerable deformation in soft substrates[19,20] and thus change morphology of the contact interface[21]. Development of soft tribology models capable of capturing these highly coupled nonlinear mechanisms is challenging and requires a thorough experimental examination of the underlying soft interface.

In this paper we focus on experimental characterization of contact area, which is one of the most important parameters of contact mechanics. In particular, our objective is to characterize the 3D, curved contact areas on soft gel substrates due to large deformation under combined normal and shear loading. A widely used method to measure contact area is based on optical interferometry, where interference fringes formed by reflected light are used to quantify the distance between contacting surfaces[14,22,23] and the zeroth-order interference fringe is interpreted as the contact area. While this method has been applied to characterize contact areas on soft materials[14], Schulze et al.[24] points out that the interferometry method may not be effective for interfaces that lack a strong mismatch of refractive index (e.g. hydrated interfaces between hydrogels). To measure contact

area of interfaces lacking strong refractive index mismatch Schulze et al.[24] developed a particle exclusion method that does not rely on interference fringes. Although both methods have enabled new experimental data revealing the contact area during normal and shear indentation of soft gels[14,24], they share a common limitation in that only a two-dimensional (2D) projection of the contact area is imaged.

In practice, the large deformation of soft materials usually renders the contact areas of a soft materials curved and three-dimensional in nature. The 3D profiles of contact area can result from either complex interface geometry (e.g. micro-patterned surface in contact with soft substrate[25,26]) or multi-axial loading (e.g. simultaneous normal and shear indentation on a soft substrate[14]), which necessitates 3D imaging to fully describe the contact interface. Recently, laser scanning confocal microscopy has been used to image the contact area between a rigid sphere and hydrogel substrates embedded with fluorescence under normal indentation[27,28]. Although confocal microscopy is capable of 3D imaging, both of these works focused only on a 2D plane that coincides with the vertical cross section of the hydrogel substrate. While Style et al.[29], Lee et al.[30] and Hall et al.[31] were able to visualize contact interfaces on gel substrates in 3D, they only considered normal indentation with passively applied load (i.e., indentation was driven by self-weight of the spherical indenter) and did not explore the effect of multiaxial loadings (e.g., in both normal and shear directions) on the 3D contact area. All these previous works[27,29–31], either 2D or 3D, considered only normal indentation and relied on the spherical shape of the indenter to identify boundary of the contact area, and thus are not easily adapted to general cases with arbitrary surface geometry and loading conditions. For example, application of shear loading may lead to non-trivial shapes of contact area even for spherical indenters on flat gel substrates. In this regard, McGhee et al.[11] presented the first work that used confocal microscopy to characterize the contact interface

between a spherical indenter and a gel substrate under steady-state sliding, which is a problem of fundamental value to soft tribology. Based on the imaging data, McGhee et al.[11] identified asymmetry in the contact area that depended on the sliding speed and correlated with the friction force of sliding. While this is a pioneering work on soft gel friction, it focused on a 2D projection of the 3D confocal images in the vertical plane along the sliding direction. In addition, the methods for image processing and determination of the contact area boundary in McGhee et al.[11] utilized the spherical geometry of the indenter. A generic method to image and identify 3D contact area on soft materials for arbitrary contact geometries and loading conditions has yet to be developed, which provides motivation for this work.

This paper introduces a micro-indentation and visualization (MIV) system capable of controlling and measuring load and displacement in normal and shear directions while enabling 3D image acquisition of the contacting bodies under fixed displacements. A method to analyze these 3D image stacks and extract boundary of the 3D contact area is also introduced to demonstrate the utility of the 3D imaging capability. This method does not rely on shapes of the contacting bodies and thus can be extended to any transparent materials. The MIV system and the image analysis method introduced in this paper will enable the correlations of 3D soft material contact interfaces with force/displacement response, thereby allowing more detailed investigation of soft contact mechanics. It should be noted that due to the limited speed of confocal imaging, we have focused on the equilibrium response of the gel substrate under quasi-static loading. Faster imaging speed would be required to capture the time-dependent behaviors under steady state sliding. Possible methods to increase the speed of confocal imaging and the corresponding trade-off in image resolution are discussed in the Results section and Supporting Information.

Methods:

MIV System Design - The MIV system is designed with the capability to precisely control normal and shear displacement, measure force along both displacement axes and enable acquisition of 3D image stacks of the contact interface on a Nikon A1R laser scanning confocal microscope (LSCM). Specifically, the design of the MIV system, shown in Figure 1, encompasses three major subsystems: 1) microscope integration frame, 2) loading subsystem for high resolution displacement control and load measurement, and 3) user interface. The aluminum microscope integration frame includes microscope mounting, specimen holder, coarse normal displacement stage (Thorlabs MVS010), and attachment to the loading subsystem. The frame design facilitates image acquisition of the contact interface in 3D during indentation experiments. The loading subsystem enables high-resolution displacement control and force measurement in both normal and shear directions. Two piezoelectric actuators are used for fine control of normal (Physik Instrumente P601.3) and shear (Physik Instrumente P611.1) displacement of the load cell and the connected indenter. A 2-axis load cell (Novatech F332-0.1) measures force in the normal and shear directions. The resolution and range of each movement and measurement system is included in Table 1. Lastly, a user interface was created in LabVIEW for manual control of the system and the ability to run tests with given parameters such as total displacement and loading rate in both directions.

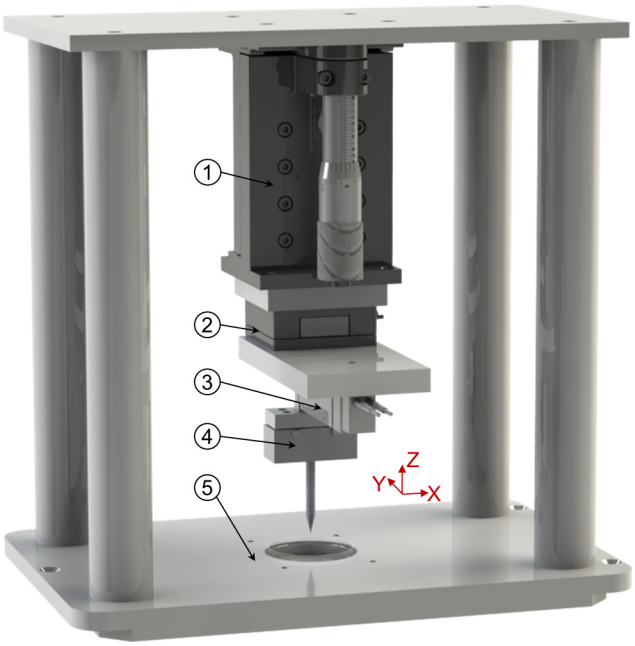

Figure 1: CAD rendering of the MIV system highlighting each component. 1) Coarse normal Z displacement stage that is used to lower the indenter into contact with the sample. 2) Fine shear displacement piezoelectric actuator. 3) Fine normal displacement piezoelectric actuator. 4) Dual axis load cell used to measure forces in normal and shear directions. 5) Microscope integration frame which allows the system to be mounted to a confocal microscope for imaging of the contact interface.

Table 1: Range and resolution of each control mechanism on the MIV system.

Component	Range	Resolution
Load Measurement X	-0.1 to 0.1 N	10 µN
Load Measurement Z	-0.1 to 0.1 N	10 µN
Displacement X	0 to 100 µm	2 nm
Displacement Z	0 to 250 µm	6 nm
Coarse Z Displacement	25.4 mm	25 µm

Indentation Microscopy – Indentation experiments were performed with polyacrylamide hydrogel substrates ~420 µm in thickness (20% total polymer content and 3% crosslinker concentration, see supporting information for details). Each hydrogel substrate, bonded to an activated coverslip, was

prepared 24 hours in advance and allowed to swell to equilibrium before the experiment. Hydrogels were submerged in deionized water throughout the entire experiment to avoid substrate dehydration and reduce adhesion effects. Green fluorescent microspheres (700 nm diameter, ThermoFisher) were embedded within the hydrogel network at a concentration of 1.65×10^8 microspheres/mL so that the deformed surface of the substrate could be reconstructed from confocal image stacks acquired during normal and shear loading. Note that we chose not to deposit the fluorescent microspheres on the top surface of the hydrogel substrate to avoid any potential modification of the hydrogel surface properties. Also, fluorescent microspheres deposited on the substrate surface may be pushed out of the contact interface upon indentation, as shown by the particle exclusion microscopy method[24]. A detailed description of the procedures to prepare the polyacrylamide substrates is included in the supporting information.

For indentation microscopy, the MIV system was integrated with the microscope stage and the hydrogel sample was loaded into the specimen holder prior to the experiment. A spherical steel indenter (radius = 250 μm) coated with a 15 μm thick red fluorescent (Rhodamine-B; see supporting information) PDMS layer was used to enable imaging of the 265 μm total radius indenter. At the beginning of the experiment, the 265 μm radius indenter, mounted to the MIV system, was manually brought into contact with the surface of a hydrogel substrate using the coarse normal displacement manipulator on the system. Quasi-static normal indentation by the piezoelectric actuator was initiated with a loading rate of 0.2 μm/s. During indentation, image stacks were acquired by a Nikon A1R LSCM using a 10X air objective (NA = 0.45). Green fluorescent microspheres (λ_{ex}:468 nm / λ_{em}:508 nm) embedded in the hydrogel were excited with a 488 nm wavelength laser and the red Rhodamine-B dye in the indenter (λ_{ex}:553 nm / λ_{em}:627 nm) was excited with a 560 nm wavelength laser. The lateral and axial resolution limits for the

LSCM can be estimated using equations (1) and (2), respectively. For these experiments, we estimate lateral resolution as 0.66 μm for the 488 nm laser or 0.76 μm for the 561 nm laser and between 3.37 μm – 4.49 μm for the 488 nm laser or 3.88 μm – 5.16 μm for the 561 nm laser since there is a refractive index mismatch in our imaging setup (η_{air} = 1, η_{water} = 1.33; see Supporting Information for details). For this experiment, one image stack was acquired in ~20 minutes, however the time resolution of the LSCM is dependent on the selected imaging parameters.

$$r_{lateral} = \frac{0.4\lambda}{NA} \tag{1}$$

$$r_{axial} = \frac{1.4\lambda\eta}{NA^2} \tag{2}$$

At every 25 μm normal indentation step, the LSCM was used to acquire an image stack through the thickness of the gel, capturing both the embedded fluorescent microspheres and the fluorescent PDMS shell of the indenter on separate channels. After the indenter achieved the maximum indentation depth, it was displaced in the shear direction at uniform increments. Image stacks were acquired at each interval for shear displacement in the same manner as those for the normal displacement.

Prior to running any indentation experiments with microscope imaging, several tests were run to demonstrate accuracy of the system. These tests included comparison between the MIV system and a commercial indentation system, system compliance measurement and correction, and load cell drift measurement. Detailed explanation of these tests and their results can be found in the supporting information. To highlight the data acquisition and continuous indentation capability of the system an indentation and shear experiment was run and the system was used to collect the

force-displacement data continuously over the entire test. Continuous indentation and shear experimental description and results are provided in supporting information.

3D Image Processing – Raw image stacks, shown in Figure 2A, captured during normal and shear loading experiments were analyzed using a custom MATLAB script to quantify the gel and spherical indenter surfaces. The raw images from each channel were filtered based on an intensity threshold to create a binary image stack. The intensity threshold used for filtering was selected based on an intensity histogram of the noise in the image stack. Binary images were then passed through a size filter that removes points without any direct neighbors in the z-direction, removing stray noise that passes through the threshold filter since fluorescent particles should be captured in multiple z-frames. Next, a triangulation of boundary points is completed for each channel in the image stacks using a built-in MATLAB function that identifies all boundary points leaving only surface points for both the hydrogel and the spherical indenter. Following this, all the boundary points that do not reside on the top surface of the hydrogel are removed from the green channel, leaving only the points that represent the top surface of the hydrogel, shown in Figure 2B.

After the image stacks are filtered and the boundary points are extracted, the image stacks are scaled by the XY pixel to micrometer ratio as well as the Z height of each plane. An additional correction was required in the Z height to account for refractive index mismatch (RIM) between the objective fluid and sample material[30]. The discrepancy between refractive index of the objective (air) and the sample (submerged hydrogel) distorts the image stacks, causing the sample to appear shorter in the z-direction than its actual height. To extract a correction factor for RIM in our experimental setup, a cylindrical fluorescent PDMS indenter was fabricated and imaged on the MIV system both through air (where RIM is not present) and through the submerged hydrogel sample (where RIM is present). Both image stacks were acquired with the same distance between

the indenter and the objective. The two image stacks are used to calculate a correction factor by dividing the height of the fluorescent cylindrical indenter from the stack imaged through air by the height of the indenter from the stack imaged through the hydrogel sample. For the experimental imaging set-up used in this paper, the RIM correction factor was calculated as 1.3, which matches well with the correction factor calculated by a group with a similar imaging set-up as Lee et. al[30]. More details of this process are provided in the supporting information. The filtered image stacks are scaled so each point location represents the actual dimensions which is a height between image planes of 0.7 μm multiplied by the RIM correction factor 1.3 and the XY pixel conversion of 2.49 μm/pixel. This process outputs a correctly dimensioned image stack that represents the hydrogel and indenter surface points shown in Figure 2B.

The correctly dimensioned image stacks were then used to identify the contact area between the spherical indenter and the hydrogel substrate. For each image stack, the distance from each green point to the nearest red point is calculated, referred to as the nearest neighbor distance (schematically shown in Figure 2D). The nearest neighbor distance within the contact area should be much smaller than the values outside the contact area. A contour plot of the nearest neighbor distance on the deformed substrate would reveal the contact area between the substrate and the indenter.

We obtain a measurement of average contact radius from the contact area identified by the nearest neighbor distance method for later comparison with theory and finite element simulation results. The radial (XY) distance from each green point to the center of the spherical indenter is calculated (see Figure 2D). The nearest neighbor distances are plotted against the XY-distances in Figure 2E. Two curves are fit through the data to find the contact radius defined by the intersection point of these curves, where the nearest neighbor distance begins to grow. The data with smaller nearest

neighbor distances is estimated as a horizontal line with y-intercept value as the average nearest neighbor distances of the 20 green points with the lowest radial distance from the center of the indenter. While the upper section of this data appears to be linear, a slight curvature can be observed when fitting a line to the data. The upper section fit is found by fitting many parabolic curves through different subsets of the data. The first curve is fit through the 20 points with the largest radial distance from the center of the indenter. Then the next largest radial distance point is added to the subset of data and a new curve is fit. One point is added for each curve fit until all points are included. Once a curve has been fit through each subset of data the curve that has the highest coefficient of determination (i.e. the R^2 value) is taken as the fit. The radial distance from the center of the indenter in an XY plane where the intersection of the two fitted lines exists is identified as the contact radius, as seen in Figure 2E.

Lastly, for qualitative investigation of the contact interface, the surface points used to extract contact radius are used for a surface fit. The green surface points are fit using a cubic piecewise interpolation and the red points are fit to a sphere, shown in Figure 2C.

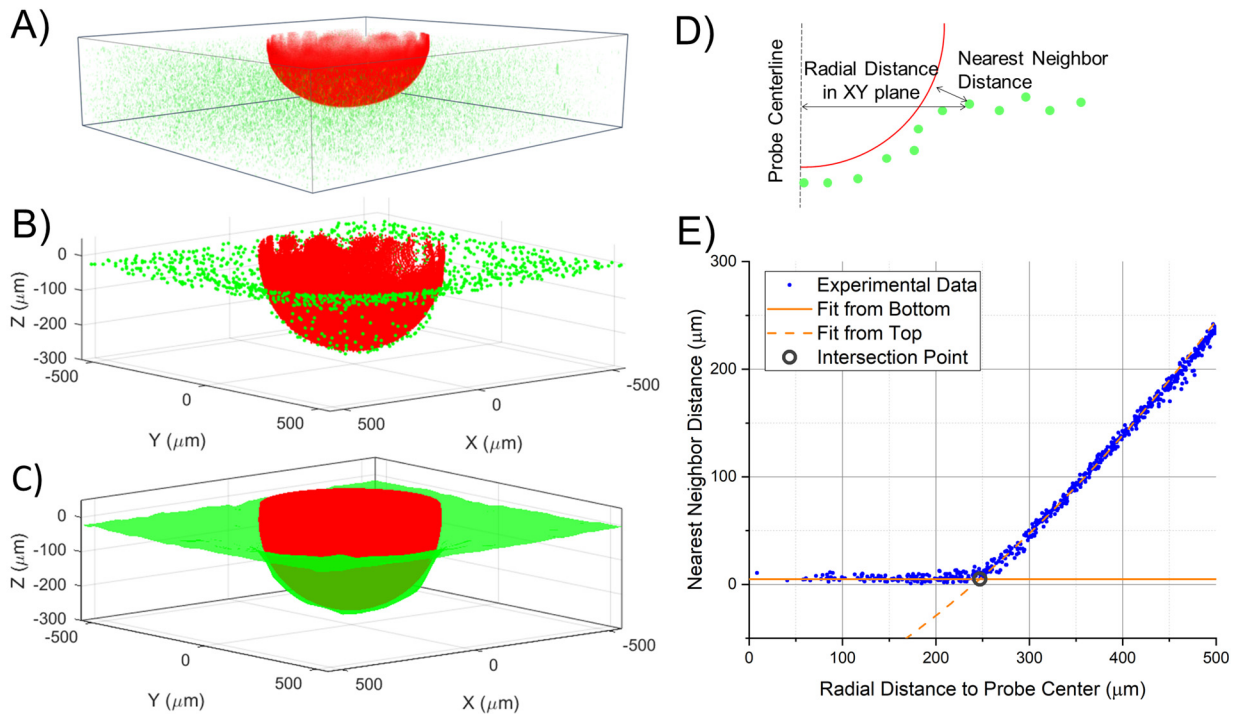

Figure 2: Representative image processing flow showing A) a 3D raw image stack of 200 μm normal indentation visualized in ImageJ[32–34], B) extracted surface points for both the spherical indenter and hydrogel surface using the image processing technique described in 3D image processing section of the text, C) hydrogel and indenter surface fits using a piecewise cubic function and sphere, respectively, D) a schematic illustrating the nearest neighbor method to determine contact area, and E) a plot of nearest neighbor distance versus radial distance from the indenter center. This plot is used to find the contact radius at the interface by identifying the intersection point between the fits for the upper and lower sections of data. At the intersection point, the radial distance from the indenter center is recorded as the experimental contact radius.

Results:

Contact Area Under Normal Indentation – Normal indentation tests were conducted to demonstrate the accuracy of the MIV system and the contact area measurement method. During normal indentation, the spherical indenter was indented into the hydrogel substrate at 25 μm increments up to a total normal displacement of 250 μm. At each increment, the indenter displacement was held fixed for approximately 9-20 minutes to allow for confocal imaging. The custom MATLAB

program described in the methods section was used for analysis of the confocal image stacks acquired during indentation. Although the indenter displacement was zeroed at the point deemed as the initial contact between the indenter and the substrate, uncertainty in the manual operation of initiating contact (see Methods section) can lead to a fixed difference between the indenter displacement and the indentation depth, defined as the distance between the indenter tip and the undeformed substrate surface (see Figure 3A). For example, in our experiment the indentation depth was found to be 9 μm deeper than the indenter displacement due to a slight initial indent at the zero-displacement position observed from the confocal images. This fixed bias of 9 μm was added to the indenter displacement to provide the correct indentation depth. Using the confocal images, we were able to determine the 3D contact area by plotting color contour of the nearest neighbor distance, as illustrated by a representative example in Figure 3B. The boundary of the contact area was defined by a threshold in the nearest neighbor distance (12 μm), which was determined by the highest nearest neighbor distance in the flat section of the nearest neighbor distance vs radial distance plot (see Figure 2E) for that image. We emphasize that the nearest neighbor distance method does not rely on the spherical profile of the indenter and thus can be used to measure 3D contact areas between soft materials with complex geometries. The time history of the prescribed indenter displacement and resultant normal force is shown in Figure 3C. Relaxation of the normal force under fixed indentation depth can be clearly observed from Figure 3C. This is attributed to the poroelastic relaxation of the hydrogel substrate[12,13,35], which will be further discussed later in this section.

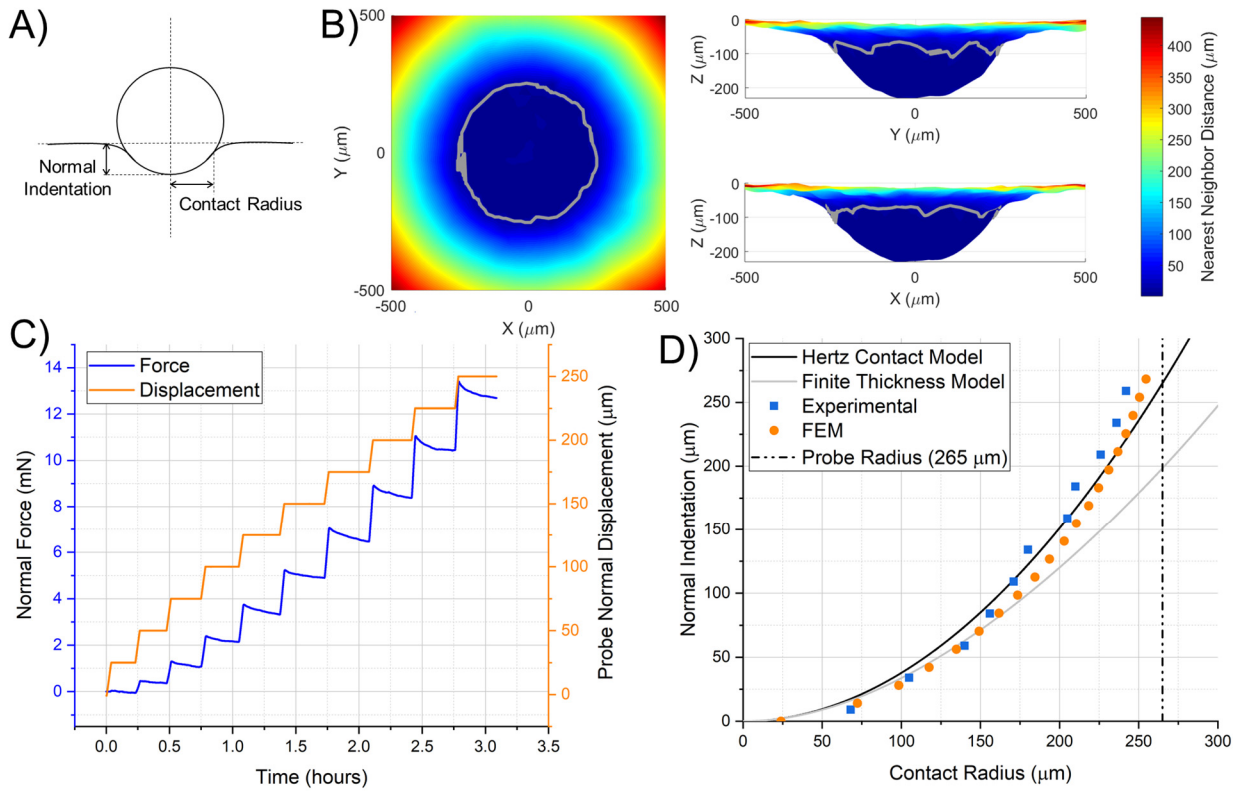

Figure 3: A) Schematic defining the indenter displacement and contact radius. B) Reconstructed hydrogel surface at maximum normal indentation in XY, XZ, and YZ views with transition line between contact and non-contact shown in gray. The color map represents nearest neighbor distance at each point, showing that this value remains low and relatively constant within the contact region, but steadily increases outside the contact region. C) Experimental data displaying both normal force and normal displacement versus time highlighting hydrogel relaxation under constant displacement during image acquisition. D) Comparison of experimentally measured contact area with finite element results, Hertz contact model[36], and finite thickness model[35].

Since projection of the 3D contact area onto the XY plane is circular (see Figure 3B), we extract the contact radius in the XY plane (see Figure 3A) using the method illustrated in Figure 2E. To demonstrate the accuracy of the experimentally measured contact radius, we compare the measurements to the Hertz contact model[36], a finite thickness corrected Hertz contact model by Hu et al.[35] and finite element (FE) simulation results in Figure 3D. According to the Hertz model, the contact radius a is given by

$$a = \sqrt{R\delta} \tag{3}$$

where δ is the indenter displacement and R is the radius of the spherical indenter (265 μm in these experiments). Note that the Hertz model assumes that the elastic substrate is infinitely thick (i.e. an elastic half-space), while in our experiments the gel substrate thickness (420 μm) can be comparable to the indentation depth (up to 259 μm). Under a given indenter displacement δ, the stronger confinement of thinner substrate can lead to larger contact radius, which can be accounted for by assigning a finite thickness correction factor to the Hertz model[35,37,38]. Here the correction factor by Hu et al.[35] is adopted:

$$a = \sqrt{R\delta}\,\frac{1.41\xi^2+0.57\xi+0.5}{\xi^2+0.49\xi+0.5}\,,\xi = \frac{\sqrt{R\delta}}{h} \tag{4}$$

where h is the thickness of the substrate. As shown in Figure 3D, for smaller indentation depths (<75 μm), the experimental contact radius is larger than predictions of the Hertz contact but matches well with the finite thickness corrected model. At higher indentation depths (>75 μm), the experimental contact radius deviates from the finite thickness corrected model and asymptotically approaches the radius of the spherical indenter. This is expected, sincethe finite thickness corrected model was solved based on linear elasticity which is not valid for deep indentation involving large deformation. For example, eq. (4) predicts a contact radius larger than the indenter radius R (265 μm) when δ > 200 μm which is physically impossible. At these deep indentations, the experimental data could be used to create more accurate models or correction factors to describe such contact interfaces. For example, we established an axisymmetric FE model using a commercial software ABAQUS to simulate the normal indentation experiment. The gel substrate was assumed to be a nearly incompressible neo-Hookean solid (Poisson's ratio = 0.495).

Frictionless contact was assumed between the indenter and the substrate. Additional details of the FE model are provided in the supporting information. Figure 3D shows that the FE simulation results, capable of capturing the nonlinear effects at deep indentation, agree better with experimental data than the Hertz or finite thickness corrected model throughout the entire range of the indentation depth (0 to 259 μm). In reality, the mechanical behaviors of the hydrogel may be more complex than a neo-Hookean solid (e.g. strain stiffening) and the contact interface may not be exactly frictionless. The experimental contact radius could provide valuable data to test more sophisticated constitutive models for the hydrogel substrate or the interface.

The contact models (i.e., Hertz, finite thickness corrected and FE) cited above all treated the hydrogel as an elastic solid. However, stress relaxation in the hydrogel is clearly evident in the time history of indentation force (see Figure 3C). The relaxation is attributed to the poroelastic nature of the hydrogel[12,13,35]. During the fast loading of a displacement increment (~2 minutes), the hydrogel behaves approximately as an incompressible elastic solid. The uneven osmotic pressure due to indentation causes migration of water molecules and hence results in stress relaxation during confocal imaging (e.g., the 9-20 minutes). If relaxation time is sufficiently large, the hydrogel approaches a compressible elastic solid with a Poisson's ratio ν less than 0.5. The poroelastic relaxation between a spherical indenter and a hydrogel substrate has been analyzed by Hu et al.[35] for small indentation depth. It was found that the fully relaxed indentation force reduces to $1/(2-2\nu)$ times the initial force, while contact radius a remains constant during relaxation. For deep indentations, instead of directly simulating poroelastic relaxation, we compared the FE results of two cases where the hydrogel substrate was modeled as either an incompressible neo-Hookean solid or a compressible one (see supporting information) and found no significant difference in contact radius. Therefore, we conclude that the contact radius is not affected by

poroelastic relaxation during normal indentation, which explains why our experimental data matches well with elastic contact models in Figure 3C.

Finally, the main source of experimental error results from the fact that the fluorescent particles were embedded in the bulk of the hydrogel substrate rather than its surface. We adopted this approach because flooding the surface with particles may affect the surface properties of the gel, and ultimately friction, during shear experiments discussed in the next section. However, it also means that when extracting contact radius, we are not using the true surface of the gel, but instead particles in the gel that are near the surface. Based on the density of fluorescent particles in the hydrogel substrate, the average distance between adjacent particles is estimated to 18 μm, which can explain the non-smooth boundary of the 3D contact area in Figure 3B. The ~18 μm average distance between particles is a potential source of error for this measurement technique because the particles could be up to 18 μm from the surface of the hydrogel. If this is the case, this method measures a larger contact radius than exists. However, this potential source of error could be reduced by increasing the density of particles embedded in the hydrogel and therefore, decreasing the average distance between identified surface particles and the actual surface of the hydrogel. See Supporting Information for more details about repeatability of the experimental method.

Contact Area Under Shear Displacement – Friction between soft bodies is a complex and poorly understood problem in the field of contact mechanics. The use of the MIV system allows for the collection of data critical to describing friction between contacting soft bodies. To investigate this interface a total of seven shear displacement steps along the positive X-direction were applied, all at a fixed normal indentation of 259 μm. The time histories of prescribed shear displacement and resulting shear force are shown in Figure 4A. For each increment of shear displacement, the corresponding shear force first increases to approximately 0.4-0.6 mN and then relaxes almost to

zero after the 20-minute 3D image acquisition. The surface profile of the deformed hydrogel substrate was reconstructed from each image volume for quantitative investigation of the contact interface (see Figure 4C and 4D). The surfaces show that as shear displacement is increased (up to 100 μm), the lateral profile of the deformed gel surface in the XZ-plane remains symmetric, as demonstrated by folding the surface profile about the central axis of the indenter. In addition, when projected onto the XY-plane, the contact area is found to be circular regardless of the magnitude of shear displacement. The size of the circular contact area, measured by the contact radius, a, obtained following Figure 2E, is approximately constant for all shear displacement increments (see Figure 4B). Given the long time (~20 minutes) required for confocal imaging at each shear displacement and the fact that images were taken from the bottom of the gel substrate to the top, the gel is expected to be in a relaxed state by the time the upper planes of gel substrate surface were imaged. Therefore, the imaged contact area should be interpreted as the contact for the relaxed state. The symmetry and constant size of the relaxed contact area corroborate well with the result that no significant shear force is observed at the relaxed state.

The results above suggest that friction between the spherical indenter and gel substrate is a rate-dependent quantity. During the fast loading stage, the applied shear displacement can result in a significant friction force. Over a longer time scale, the friction force reduces substantially under a fixed shear displacement due to relaxation of the gel substrate. The friction force after the gel fully relaxes is negligible as compared to its value before relaxation, even at deep normal indentation where half of the spherical indenter is below the undeformed gel surface (i.e. at indentation depth of 259 μm). This is in contrast to normal indentation where the fully relaxed indentation force is comparable to the unrelaxed value. In addition, the corresponding contact area at the relaxed state remains unchanged even upon shear displacement. To support the experimental observations of

near-zero shear force and constant contact area at the relaxed state upon combined deep normal indentation and shear, we perform FE simulations where the gel substrate is modeled as a compressible neo-Hookean solid to capture its fully relaxed state (see supporting information for details). The contact interface between the indenter and the gel substrate is assumed to be frictionless for two reasons. First, our experiments were performed submerged and a water layer is expected to be present at the interface. Second, during image acquisition, the shear displacement was held fixed and thus no sliding is expected for the fluid layer. Using the FE model, we find that resistance force to shear displacement is below 0.01mN, which practically zero as compared to the unrelaxed shear force (approximately 0.4-0.6 mN) measured in experiments. Also, the FE simulation results suggest that the contact area remains constant even when a large shear displacement is applied. Both results agree with our experimental observations at the relaxed state.

To put our findings into perspective, we note that shear indentation experiments with rigid spherical indenters and hydrogel substrates have been performed in the literature to investigate friction under steady state shear sliding[11,14]. Specifically, McGhee et al.[11] observed asymmetry in the lateral cross-section of the deformed gel surface (equivalent to the XZ-plane plot in Figure 4C and 4D). The extent of asymmetry decreases with the sliding speed and so does the friction coefficient. Delavoipiere et al.[14] also observed asymmetry of the contact area, but in the XY-plane, when the sliding speed is above a threshold. At sliding speeds lower than this threshold, the contact area remains circular and maintains a constant size independent of the sliding speed. The dependence of contact area asymmetry on sliding speed is due to poroelastic relaxation of the gel substrate, as demonstrated by an analytical model in Delavoipiere et al.[14]. Both works are consistent with the absence of contact area asymmetry in our data, given that the contact area imaged in our work corresponds to the relaxed state of the gel or the slow end of the sliding speed

spectrum. Presumably the contact area and gel deformation may be asymmetric during the fast loading stage of our experiment, but capturing such profile would require a much faster 3D imaging technique, which is beyond the scope of this work. However, there are several imaging parameters that could be adjusted to decrease image acquisition time including image stack height, z-step size, and decreasing XY scan size focusing only on specific regions of interest. Additionally, there are other techniques like employing a resonant scanner or a spinning disk confocal which could also decrease image acquisition time for more dynamic experiments. Even though these adjustments would increase the time resolution of this method, there is often a decrease in image resolution associated with these techniques. This could be a challenging factor in data analysis, but the lower resolution images may still be adequate for investigating contact during shear sliding depending on the parameters of interest. See Supporting Information for more details about tradeoffs between image acquisition time and corresponding image resolution.

Even though our experimental observations agree with previous literature, we emphasize that the indentation depth in our experiments (i.e., half of the sphere is below the undeformed gel surface) is much larger than those in the literature[11,14]. The large indentation depth generated a deep dimple on the gel substrate, which translates as the applied shear displacement increases. The near-zero shear force at the relaxed state confirms that there cannot be any adhesive interaction on the interface. More importantly, it also suggests that the dimple due to the large indentation depth does not provide any resistance to global shear displacement by local lateral contact between the indenter and the deformed gel substrate. In contrast, when indenters with other geometry, such as a cylindrical punch or a pyramid, are indented into a hydrogel substrate and then sheared, normal contact between lateral surface of the punch or pyramid and the deformed gel substrate can lead to asymmetric contact area and a net friction force even at the fully relaxed state of the gel

substrate. More information about utilization of the nearest neighbor distance method for arbitrary indenter geometry is provided in the Supporting Information. Investigation on this mechanism of local lateral contact and the consequent static friction is ongoing and will be reported in a future work.

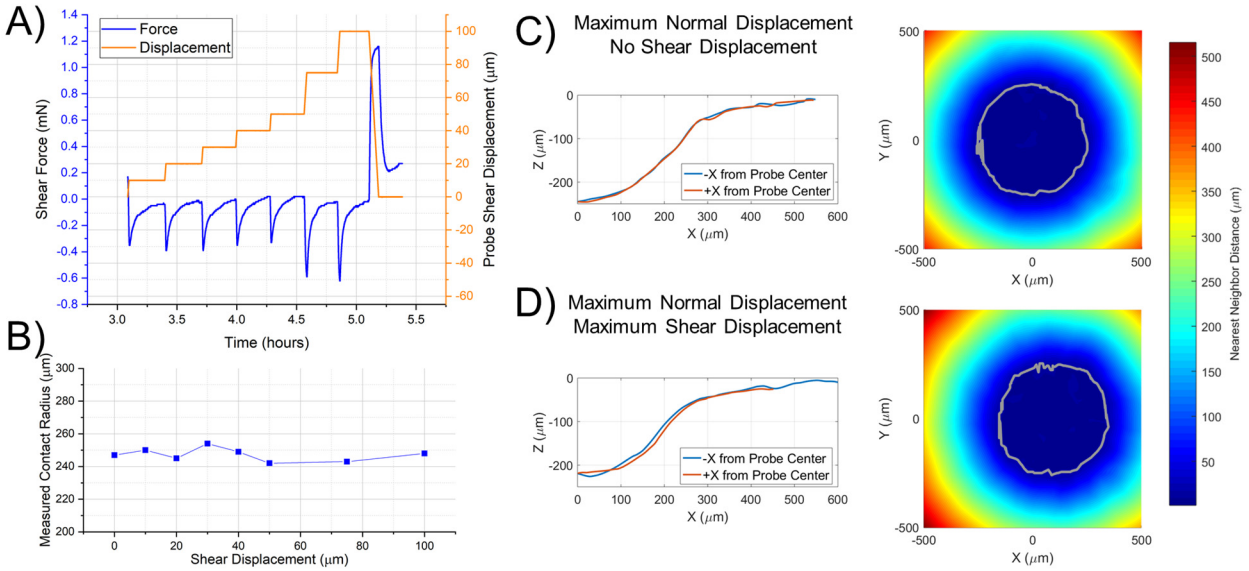

Figure 4: A) Experimental data displaying both shear force and shear displacement versus time highlighting hydrogel relaxation under constant shear displacement during image acquisition. B) Measured contact radius versus shear displacement. C) Data extracted from the image stack acquired at maximum normal displacement and zero shear displacement. D) Data extracted from the image stack acquired at maximum normal displacement and maximum shear displacement. For both C and D the left graph shows a 2D slice of the hydrogel surface along the XZ plane, folded on itself at the center of the spherical indenter. The graph on the right shows a top-down view of the hydrogel surface along the XY plane with the color map representing the nearest neighbor distance at each point and transition line between contact and non-contact shown in gray.

Conclusion:

This paper introduces a micro-indentation and visualization (MIV) system which allows for shear and normal indentation and force measurements while simultaneously providing the ability to image the contact interface in 3D on a laser scanning confocal microscope. Validation of the system is carried out to ensure accurate measurement of load and displacement compared to a commercially available indentation system. A classic contact test where a rigid spherical indenter is indented into a flat soft substrate was completed to investigate the use of 3D imaging to find contact area. During this test, force and displacement data were collected along with 3D images at various indentation depths. A new method to measure contact area in 3D was introduced and used to measure contact radius for each image stack. The nearest neighbor distance method introduced can be used as a general method to find contact of more complex interfaces because it relies only on 3D points in space. The contact radius measured was compared to elastic contact models and FE simulation. From the results, we observe that at high indentation depths both the Hertz model and finite thickness corrected model cannot accurately capture the contact radius. Thus, this experimental method could be used to create new contact models or correction factors on current models to better describe extreme contact cases. The MIV system was also used to run shear displacement experiments. The shear force measured during imaging of the interface relaxes to almost zero. Meanwhile, the 3D contact area constructed from 3D confocal image stacks exhibits a symmetric 3D profile regardless of the magnitude of applied shear displacement. Such symmetric contact area and relaxed shear force agree well with previous observations of steady state sliding with low velocities[14]. The ability of our method to reconstruct the contact area in 3D will allow more detailed investigation of contact interfaces in soft materials than 2D imaging, especially when complex contact geometry is involved. Therefore, the test system and image processing

method introduced in this paper will be useful for further investigation of soft material contact mechanics.

Acknowledgements

The authors would like to thank the National Science Foundation (NSF) for funding this work through grant CMMI-1636203. The imaging work was performed at the BioFrontiers Institute Advanced Light Microscopy Core Facility with helpful advice from Joe Dragavon. Laser scanning confocal microscopy was performed on a Nikon A1R microscope supported by NIST-CU Cooperative Agreement award number 70NANB15H226. The authors would like to thank the Biomechanics and Biomimetics Lab for use of the Hysitron TI-950 Nanoindentor and Kevin Eckstein for his technical assistance.

Supplemental Information

There are two supporting information files attached to this manuscript. The first is a PDF that covers material preparation procedures, system characterization, finite element analysis and refractive index mismatch correction. The second is a video showcasing the 3D experiments and results that are hard to capture on a 2D manuscript.

References

1. Bhushan, B. Contact mechanics of rough surfaces in tribology: multiple asperity contact. *Tribol. Lett.* **4**, 1–35 (1998).
2. Tichy, J. A. & Meyer, D. M. Review of solid mechanics in tribology. *Int. J. Solids Struct.* **37**, 391–400 (2000).

3. Priest, M. & Taylor, C. M. Automobile engine tribology — approaching the surface. *Wear* **241**, 193–203 (2000).
4. Britton, R. D., Elcoate, C. D., Alanou, M. P., Evans, H. P. & Snidle, R. W. Effect of Surface Finish on Gear Tooth Friction. *J. Tribol.* **122**, 354–360 (1999).
5. Pitenis, A. A. *et al.* Challenges and opportunities in soft tribology. *Tribol. - Mater. Surf. Interfaces* **11**, 180–186 (2017).
6. Alcaide, J. O., Pearson, L. & Rentschler, M. E. Design, modeling and control of a SMA-actuated biomimetic robot with novel functional skin. in *2017 IEEE International Conference on Robotics and Automation (ICRA)* 4338–4345 (2017). doi:10.1109/ICRA.2017.7989500
7. Li, F., Wang, A. & Wang, C. Analysis of friction between articular cartilage and polyvinyl alcohol hydrogel artificial cartilage. *J. Mater. Sci. Mater. Med.* **27**, 87 (2016).
8. Timan Idriss Gasab, M. *et al.* Advanced DLC coating technique on silicone-based tubular medical devices. *Surf. Coat. Technol.* **307**, 1084–1087 (2016).
9. Sliker, L. J., Kern, M. D., Schoen, J. A. & Rentschler, M. E. Surgical evaluation of a novel tethered robotic capsule endoscope using micro-patterned treads. *Surg. Endosc.* **26**, 2862–2869 (2012).
10. Greenwood, J. A. & Tabor, D. The Friction of Hard Sliders on Lubricated Rubber: The Importance of Deformation Losses. *Proc. Phys. Soc.* **71**, 989–1001 (1958).
11. McGhee, E. O. *et al.* In Situ Measurements of Contact Dynamics in Speed-dependent Hydrogel Friction. *Biotribology* **13**, 23–29 (2018).
12. Hu, Y., Zhao, X., Vlassak, J. J. & Suo, Z. Using indentation to characterize the poroelasticity of gels. *Appl. Phys. Lett.* **96**, 121904 (2010).

13. Chan, E. P., Hu, Y., Johnson, P. M., Suo, Z. & Stafford, C. M. Spherical indentation testing of poroelastic relaxations in thin hydrogel layers. Soft Matter 8, 1492–1498 (2012).
14. Delavoipière, J. *et al.* Friction of Poroelastic Contacts with Thin Hydrogel Films. *Langmuir* **34**, 9617–9626 (2018).
15. Reale, E. R. & Dunn, A. C. Poroelasticity-driven lubrication in hydrogel interfaces. Soft Matter 13, 428–435 (2017).
16. Lin, D. C., Shreiber, D. I., Dimitriadis, E. K. & Horkay, F. Spherical indentation of soft matter beyond the Hertzian regime: numerical and experimental validation of hyperelastic models. *Biomech. Model. Mechanobiol.* **8**, 345 (2008).
17. Duan, Z., An, Y., Zhang, J. & Jiang, H. The effect of large deformation and material nonlinearity on gel indentation. *Acta Mech. Sin.* **28**, 1058–1067 (2012).
18. Nguyen, D. T. *et al.* Surface Pressure and Shear Stress Fields within a Frictional Contact on Rubber. *J. Adhes.* **87**, 235–250 (2011).
19. Wang, Y., Dhong, C. & Frechette, J. Out-of-Contact Elastohydrodynamic Deformation due to Lubrication Forces. *Phys. Rev. Lett.* **115**, 248302 (2015).
20. Wang, Y., R. Tan, M. & Frechette, J. Elastic deformation of soft coatings due to lubrication forces. *Soft Matter* **13**, 6718–6729 (2017).
21. Wang, Y. & Frechette, J. Morphology of soft and rough contact via fluid drainage. *Soft Matter* **14**, 7605–7614 (2018).
22. Krick, B. A., Vail, J. R., Persson, B. N. J. & Sawyer, W. G. Optical In Situ Micro Tribometer for Analysis of Real Contact Area for Contact Mechanics, Adhesion, and Sliding Experiments. *Tribol. Lett.* **45**, 185–194 (2012).

23. Ovcharenko, A., Halperin, G., Etsion, I. & Varenberg, M. A novel test rig for in situ and real time optical measurement of the contact area evolution during pre-sliding of a spherical contact. *Tribol. Lett.* **23**, 55–63 (2006).
24. Schulze, K. D., Bennett, A. I., Marshall, S., Rowe, K. G. & Dunn, A. C. Real Area of Contact in a Soft Transparent Interface by Particle Exclusion Microscopy. *J. Tribol.* **138**, 41404-41404–6 (2016).
25. Kern, M. D., Long, R. & Rentschler, M. E. A representative volume element model for the adhesion between a micro-pillared surface and a compliant substrate. *Mech. Mater.* **119**, 65–73 (2018).
26. Kern, M. D., Qi, Y., Long, R. & Rentschler, M. E. Characterizing Adhesion between a Micropatterned Surface and a Soft Synthetic Tissue. *Langmuir* **33**, 854–864 (2017).
27. Schulze, K. D. *et al.* Polymer Osmotic Pressure in Hydrogel Contact Mechanics. *Biotribology* **11**, 3–7 (2017).
28. Pham, J. T., Schellenberger, F., Kappl, M. & Butt, H.-J. From elasticity to capillarity in soft materials indentation. *Phys. Rev. Mater.* **1**, 15602 (2017).
29. Style, R. W., Hyland, C., Boltyanskiy, R., Wettlaufer, J. S. & Dufresne, E. R. Surface tension and contact with soft elastic solids. *Nat. Commun.* **4**, 2728 (2013).
30. Lee, D., Rahman, M. M., Zhou, Y. & Ryu, S. Three-Dimensional Confocal Microscopy Indentation Method for Hydrogel Elasticity Measurement. *Langmuir* **31**, 9684–9693 (2015).
31. Hall, M. S., Long, R., Hui, C.-Y. & Wu, M. Mapping Three-Dimensional Stress and Strain Fields within a Soft Hydrogel Using a Fluorescence Microscope. *Biophys. J.* **102**, 2241–2250 (2012).

32. Schindelin, J. *et al.* Fiji: an open-source platform for biological-image analysis. *Nat. Methods* **9**, 676–682 (2012).

33. Schmid, B., Schindelin, J., Cardona, A., Longair, M. & Heisenberg, M. A high-level 3D visualization API for Java and ImageJ. *BMC Bioinformatics* **11**, 274 (2010).

34. Schneider, C. A., Rasband, W. S. & Eliceiri, K. W. NIH Image to ImageJ: 25 years of image analysis. *Nat. Methods* **9**, 671–675 (2012).

35. Hu, Y., Chan, E. P., Vlassak, J. J. & Suo, Z. Poroelastic relaxation indentation of thin layers of gels. *J. Appl. Phys.* **110**, 86103 (2011).

35. Johnson, K. L. Contact Mechanics. (Cambridge University Press, 1987).

37. Shull, K. R., Ahn, D., Chen, W.-L., Flanigan, C. M. & Crosby, A. J. Axisymmetric adhesion tests of soft materials. *Macromol. Chem. Phys.* **199**, 489–511 (1998).

38. Shull, K. R. Contact mechanics and the adhesion of soft solids. *Mater. Sci. Eng. R Rep.* **36**, 1–45 (2002).

39. Fischer, R. S., Myers, K. A., Gardel, M. L. & Waterman, C. M. Stiffness-controlled three-dimensional extracellular matrices for high-resolution imaging of cell behavior. *Nat. Protoc.* **7**, 2056–2066 (2012).

40. Denisin, A. K. & Pruitt, B. L. Tuning the Range of Polyacrylamide Gel Stiffness for Mechanobiology Applications. *ACS Appl. Mater. Interfaces* **8**, 21893–21902 (2016).

For Table of Contents only:

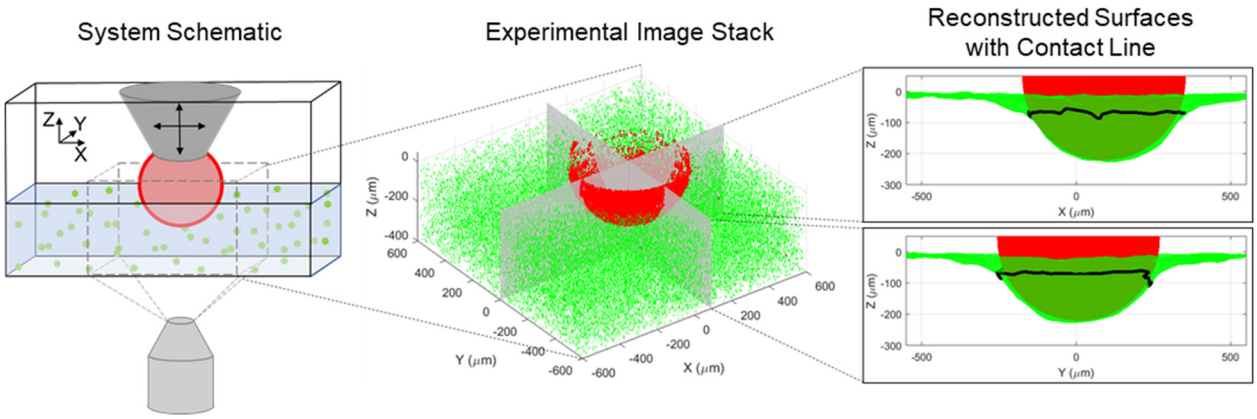

Supporting Information

Three-Dimensional Microscale Imaging and Measurement of Soft Material Contact Interfaces Under Quasi-Static Normal Indentation and Shear

Karl G. Johannes[*], *Kristin N. Calahan*[*], ([*]: equal contributions) *Yuan Qi, Rong Long, Mark E. Rentschler*

Department of Mechanical Engineering, University of Colorado, Boulder

E-mail: karl.johannes@colorado.edu

The supporting information provided covers detailed descriptions and figures describing material preparation, system characterization, finite element analysis and refractive index mismatch correction.

Materials

Hydrogel Preparation - Activated coverslips were prepared by first washing with 0.1M NaOH following by rinsing with deionized water. Next, the coverslips were soaked in a 0.5% (3-aminopropyl) trimethoxysilane solution at room temperature for 30 minutes with gentle agitation on a shaker plate. After coverslips were washed in six changes of deionized water, the coverslips

were dried in an oven (~30 minutes, 50 °C). When the coverslips were cooled to room temperature, they were immersed in a 0.5% glutaraldehyde (in 1X PBS) solution for 30 minutes at room temperature with gentle agitation on a shaker plate. Finally, coverslips were washed in three changes of deionized water and air-dried. Activated coverslips were stored in a desiccator for up to two months before use. This protocol was adapted from the protocol published by Fischer et al[1].

Polyacrylamide hydrogels were prepared from stock solutions of 0.5 g/mL acrylamide (Sigma-Aldrich) and 0.025 g/mL bis-acrylamide (Sigma-Aldrich) prepared in deionized water. Precursor solution was prepared by diluting required amounts of acrylamide and bis-acrylamide stock solutions with deionized water to reach the 20% total polymer content (w/v) and 3% cross-linker concentration (w/w) calculated using equations (1) and (2) from Denisin et al[2]. Gel precursor solution was mixed with fluorescent microspheres (Thermo-Fisher) to reach a final volume fraction of 4.5×10^8 microspheres/mL in the hydrogel. The precursor solution with microspheres was sonicated for 10 minutes in a sonication bath to ensure a uniform concentration of fluorescent microspheres throughout the hydrogel volume. Gelation was initiated by the addition of 25 µL of 10% w/v ammonium persulfate (APS, Sigma-Aldrich) to 4.75 mL of gel precursor solution followed by 5 µL of N,N,N',N' - Tetramethylethylenediamine accelerator (TEMED, Sigma-Aldrich). The solutions were gently mixed before pipetting onto activated coverslips and polymerized at room temperature. All gels were polymerized between one activated coverslip and another coverslip coated with Rain-X solution with a 500 µm thick silicone spacer (McMaster) in between. Following polymerization, the Rain-X coated coverslip was gently lifted from the gel surface with tweezers and the gels were stored at room temperature in deionized water for 24 hours before experiments to allow for equilibrium swelling. All gels were

submerged in deionized water during experimental testing to avoid issues with water evaporation altering hydrogel properties.

Agarose hydrogels for nanoindentation were prepared by mixing low-melt agarose (Sigma-Aldrich) with MilliQ water for a final concentration of 10% (w/v). Solution was heated in a microwave until boiling and then poured into 35 mm petri dish before gelation. Following gelation, a tissue biopsy punch (4 mm diameter) was used to punch out samples for indentation testing. Gels were left in deionized water for 24 hours at room temperature for equilibrium swelling before testing.

Fluorescent Probe Preparation - The indentation probe used for contact area experiments was an aluminum cylinder turned down on one side to a conical tip with a high precision 500 μm diameter steel ball bearing (McMaster) glued to the point of the tip. Uncured PDMS (10:1 weight ratio, Dow-Corning) was dripped over the probe held in an upright position allowing gravity to cause the material to flow down the side of the probe forming a PDMS shell around the steel ball bearing. The PDMS was heat cured in an oven at 75 °C for 8 hours before it was fluorescently dyed. The entire probe was then soaked in a 100 nM Rhodamine-B (Sigma-Aldrich) dye solution for 4 hours to ensure the rhodamine dye is absorbed into the PDMS shell for fluorescence microscopy.

Bulk Hydrogel Characterization - Polyacrylamide hydrogels were prepared with and without embedded fluorescent microspheres for bulk characterization. Gels were prepared according to the formulation described above with or without the addition of fluorescent microspheres. Instead of the 500 μm spacer between glass coverslips, a 2 mm silicone spacer (McMaster) was used to ensure that the hydrogel represented an elastic half space for bulk testing. Indentation

tests were conducted for gels containing fluorescent microspheres and those without. For each hydrogel, a probe with a 500 µm diameter sapphire sphere glued to the tip was used for indentation tests conducted on the custom-built micro-indentation and visualization (MIV) system. For each indentation test, the probe was indented 125 µm into submerged polyacrylamide gels at a loading rate of 0.25 µm/s. Submerged gels were used to avoid water evaporation from the gel during testing. Each test was initiated 25 µm in the x-direction from the last indent for a total of four indents per gel. In Figure S1, we can see the addition of fluorescent particles has a stiffening effect on the gel. This discrepancy has no effect on the data presented in this paper as all of the experimental data was collected using hydrogels with embedded particles. However, it is useful information since a different experimental design could require specific stiffness gels so the inclusion of microparticles would need to be accounted for in those cases.

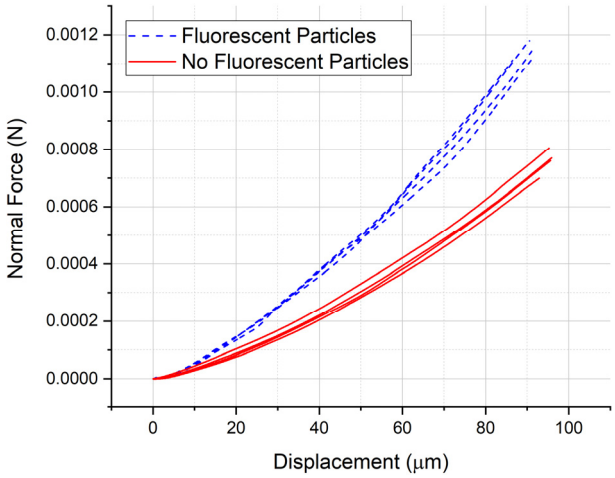

Figure S1: Force-displacement curves for bulk characterization of hydrogels embedded with fluorescent particles and hydrogels without embedded particles.

System Characterization

Drift Characterization & Load Cell Accuracy Measurement - Measurement drift of the MIV

system was characterized in both the normal and shear directions by adding washers, of known mass, to the load cell and monitoring system measurements over 10 minutes. Prior to testing, the load cell is turned on and allowed 30 minutes to equilibrate and warm-up before recording any data. Figure S2A shows the drift and accuracy data for the normal direction with each calibration trial shown in a colored solid line and the known mass values shown as black dotted horizontal lines. All trials show that the load cell is properly measuring force, within the repeatability and creep ratings of the load cell.

Figure S2B shows measurement accuracy and drift data for shear measurements at the force center of the load cell. The data shows that the load cell drift for shear measurement follows the same pattern as the normal measurement, leveling out very quickly after calibration weight additions. Both the normal and shear load measurements are found to be within the published load cell tolerances.

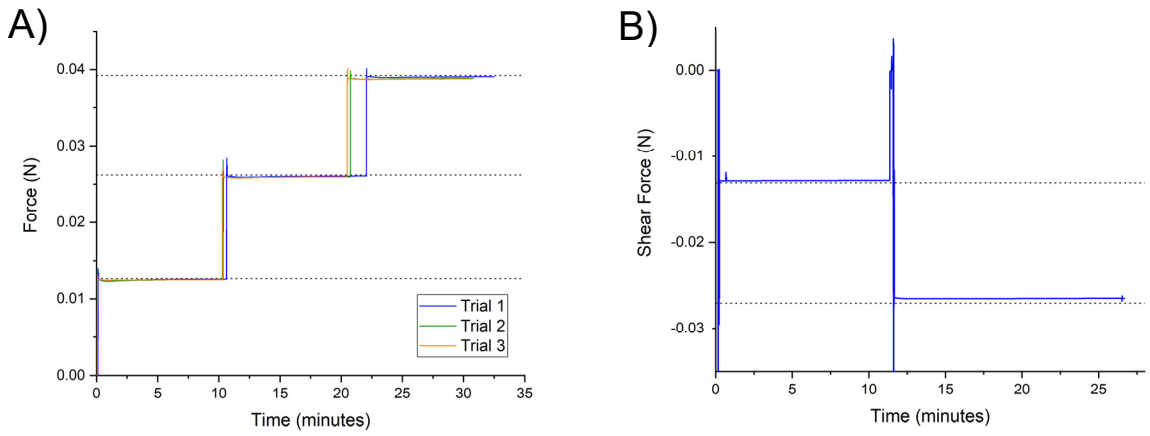

Figure S2: (A) Normal force drift and calibration over time. Black dotted lines correspond to calibration weights. (B) Shear force drift and calibration data over time. Black dotted lines correspond to calibration weights.

Machine Compliance Characterization - For normal machine compliance characterization, a spherical sapphire probe (500 µm diameter) was indented into glass using the piezoelectric

actuators on the MIV system. The deformation measured and shown in the load versus displacement curve in Figure S3A shows the compliance of the load cell in the normal direction. The slope of the fitted line was used to correct all data sets for machine compliance by assuming the load cell acts as a spring in an otherwise rigid system. The slope can be used to calculate the actual displacement of the probe during experiments accounting for compression of the load cell.

Shear compliance was measured in a similar way by displacing a probe in the shear direction into a rigid block of material. Just as for the normal case, the slope of the fitted line was used to correct all data sets for compliance in the shear direction. For the experimental data presented in this paper, the machine compliance corrected the displacement results by a maximum of 2 µm in the normal direction and less than 1 µm in the shear direction.

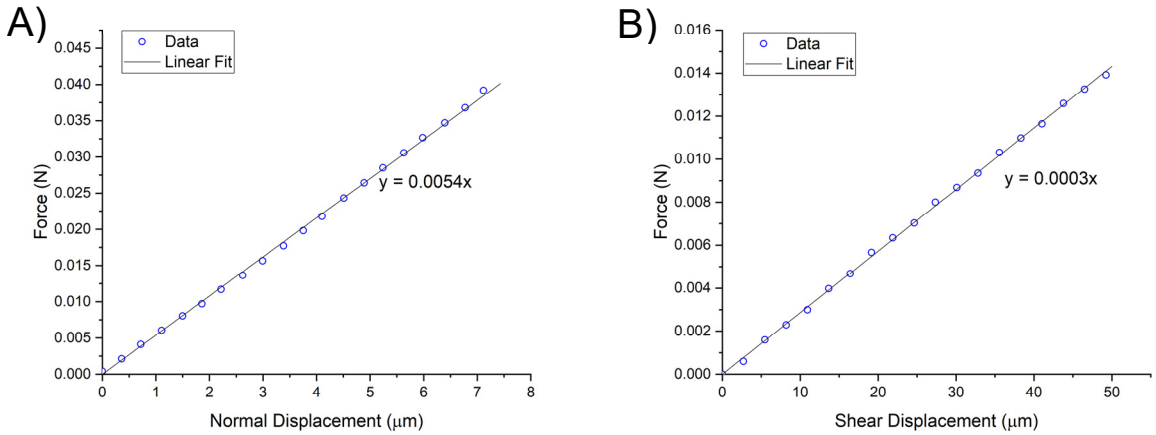

Figure S3: (A) Normal force-displacement data for machine compliance measurement correction. The slope of the linear fit was used to calculate the displacement correction applied to experimental data. (B) Shear force-displacement data for machine compliance measurement.

MIV System Validation - To validate the force and displacement capabilities of the system, a normal indentation test was run on our system and a commercial nanoindentation system (Hysitron TI-950). In both tests, the probe material and size (500 µm diameter spherical sapphire probe), loading rate (0.25 µm/s) and total displacement (125 µm), and the hydrogel sample (10% w/v

agarose gel) were the same. Five tests were conducted on each system, each at a different location on the sample. Each test was fit to a Hertz indentation curve to find an elastic modulus value for substrate material. The five modulus values for each respective machine were then averaged to find a mean modulus value for the hydrogel sample. In Figure S4, a Hertz curve using the average modulus value calculated from the tests on the MIV system is plotted alongside the average curves with standard deviations from each system. These results show no statistically significant difference by using a t-test comparing the estimated modulus values from each test between the two systems (p-value = 0.6082). This result demonstrates that the MIV system can accurately measure force and displacement for normal indentation tests comparable to a commercially available indentation system.

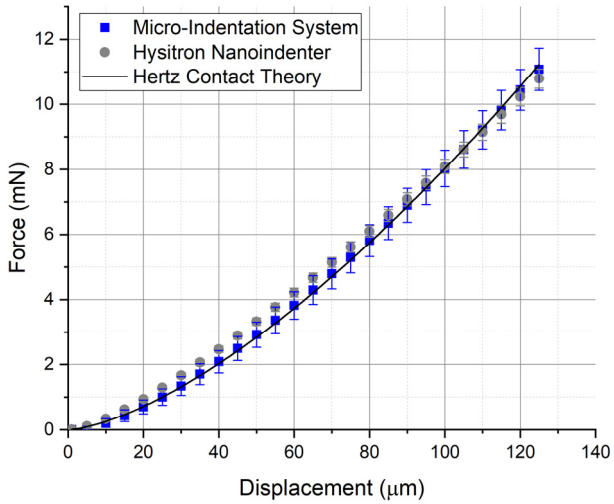

Figure S4: Comparison of force-displacement data from normal indentation tests using the MIV system (blue) versus a Hysitron TI 950 Nanoindenter (grey) versus Hertz Contact Theory (black). The average values of five indentation tests are shown with standard deviation for each system. The theoretical Hertzian contact model curve is given by the elastic modulus equal to the average of the fitted estimated elastic modulus values for the indentation tests using the MIV system.

Continuous Indentation Experiments - The MIV system can take continuous data as shown in Figure S5. The force versus displacement curves here show the capability of the system in

capturing data without waiting times and relaxation during image acquisition. In the shear displacement graph, there is an obvious stick-slip behavior that the curve follows while under shear loading, showing the utility of this system to accurately measure microscale friction parameters.

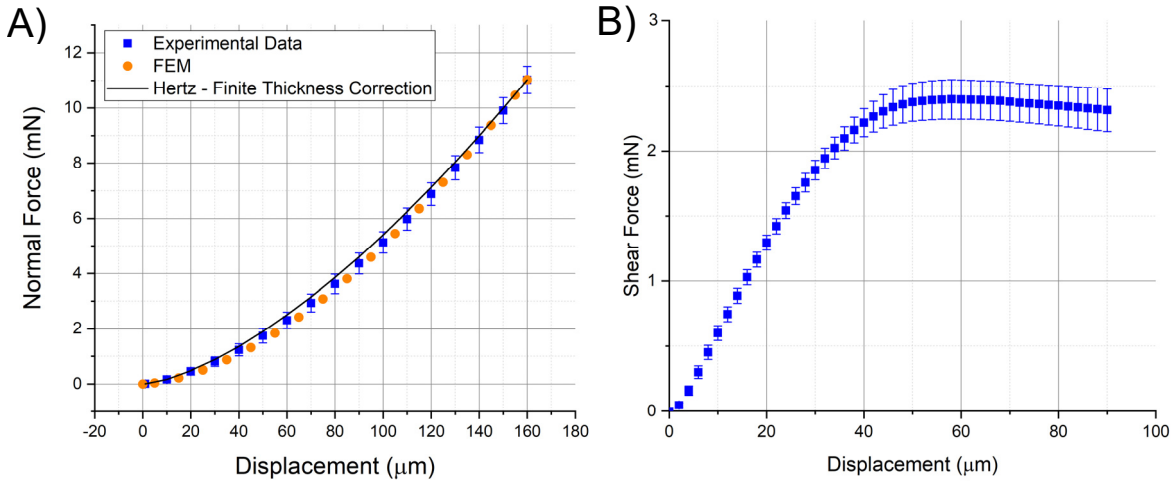

Figure S5: (A) Experimental force displacement data of normal indentation with modulus fitted FEM and Hertz finite thickness corrected theory. (B) Plot of measured shear force vs shear displacement.

Finite Element Simulation

Axisymmetric Normal Indentation – Finite Element (FE) simulations were run in ABAQUS (version 2017, Simulia, Dassault Systèmes, Providence, RI) to simulate the indentation process. Due to symmetry, the 3D model is simplified to an axisymmetric model as shown in Figure S6 in which the bottom surface of the substrate is fixed and a symmetric boundary condition is applied to the left side. The spherical steel probe is modelled as a rigid shell and is tied with inner side of the PDMS coating with uniform thickness. Geometry of the FE model is set to be the same as the experiment, i.e. radius of steel ball R = 250 μm, thickness of PDMS coating t_0 = 15 μm and thickness of the gel substrate h_0 = 420 μm. The width of the gel substrate was set to be w_0 = 1500 μm that is far larger than the radius of the steel ball to exclude boundary effect. The bulk property

of both the PDMS coating and gel substrate were modeled as nearly incompressible (Poisson's ratio =0.495) neo-Hookean solid with Young's modulus E_{PDMS}= 9.0 MPa and E_{gel} = 75.0 kPa, respectively. The contact between the outer surface of the PDMS and the hydrogel substrate is assumed to be frictionless. To achieve deeper indentation, a dynamic explicit solver was used and a velocity loading of v = 0.01 mm/s was applied on the reference point (red dot in Figure S6) of the steel ball to simulate a quasi-static indentation process.

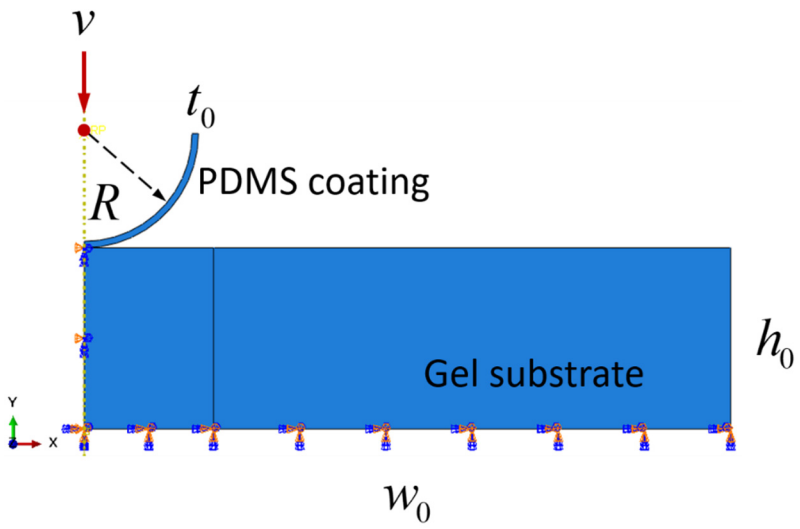

Figure S6: Finite element geometry and boundary conditions used for normal indentation simulation.

Effect of Poisson's Ratio on Contact Area – As discussed in the main text, the gel substrate undergoes poroelastic relaxation at long time scales. After full relaxation, the gel substrate should be considered as a compressible solid instead of the incompressible solid assume above. From our normal indentation data (see Figure 3C in the main text), the indentation force after relaxation reduces to approximately 80%~90% of the unrelaxed indentation force. According to Hu et al.[3], the ratio between the fully relaxed indentation force and the unrelaxed indentation force is $1/(2-2\nu)$, where ν is the Poisson's ratio of the fully relaxed gel. Based on this result,

we estimate the Poisson's ratio of the relaxed gel substrate to be 0.4 to 0.45. To check the effect of Poisson's ratio on the contact area, we performed an additional simulation using the axisymmetric model where the gel substrate was modeled as a compressible neo-Hookean solid with Young's modulus E_{gel} = 75.0 kPa and bulk modulus K_{gel} = 116.7 kPa (corresponds to Poisson's ratio = 0.4). The contact radius vs displacement data from these two simulations are shown in Figure S7. As discussed in the main text, the change in Poisson's ratio has no significant effect on the contact radius seen in simulations. Since the contact area is not a function of the compressibility of the gel, this allows us to use incompressible material for the half symmetry simulation used to simulate shear.

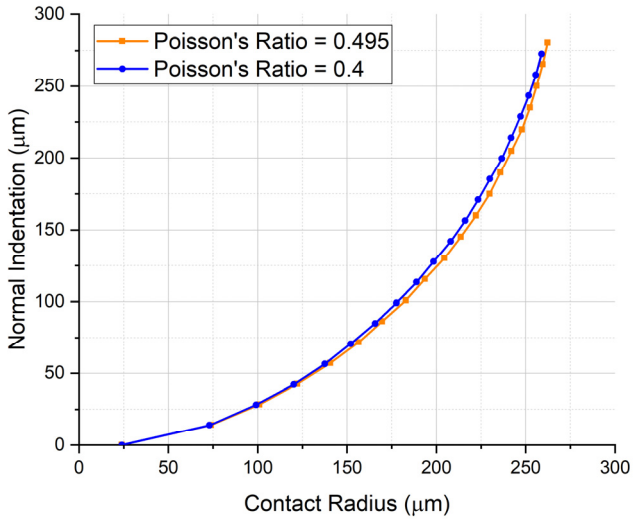

Figure S7: Finite element contact area versus probe displacement for two different Poisson's ratios. It can be seen that the substrate being compressible has a negligible effect on the contact area through the indentation.

Half Symmetry Indentation and Shear - To simulate the shear loading phase, we built a 3D model with symmetry boundary conditions, shown in Figure S8. All parameters were the same as the axisymmetric model except that the gel substrate was modeled as a compressible neo-Hookean solid with Young's modulus E_{gel} = 75.0 kPa and bulk modulus K_{gel} = 116.7 kPa (corresponds to Poisson's ratio = 0.4). We applied a shear velocity of 0.01 mm/s along negative

x-direction after the maximum indentation and kept the maximum indentation during shear. The gel substrate was meshed into 55260 C3D8R elements. FE simulation of shear loading at the hydrogel interface agree with the experimental results presented in this paper that under quasi-static loading a spherical probe does not hold shear force and the contact area remains constant.

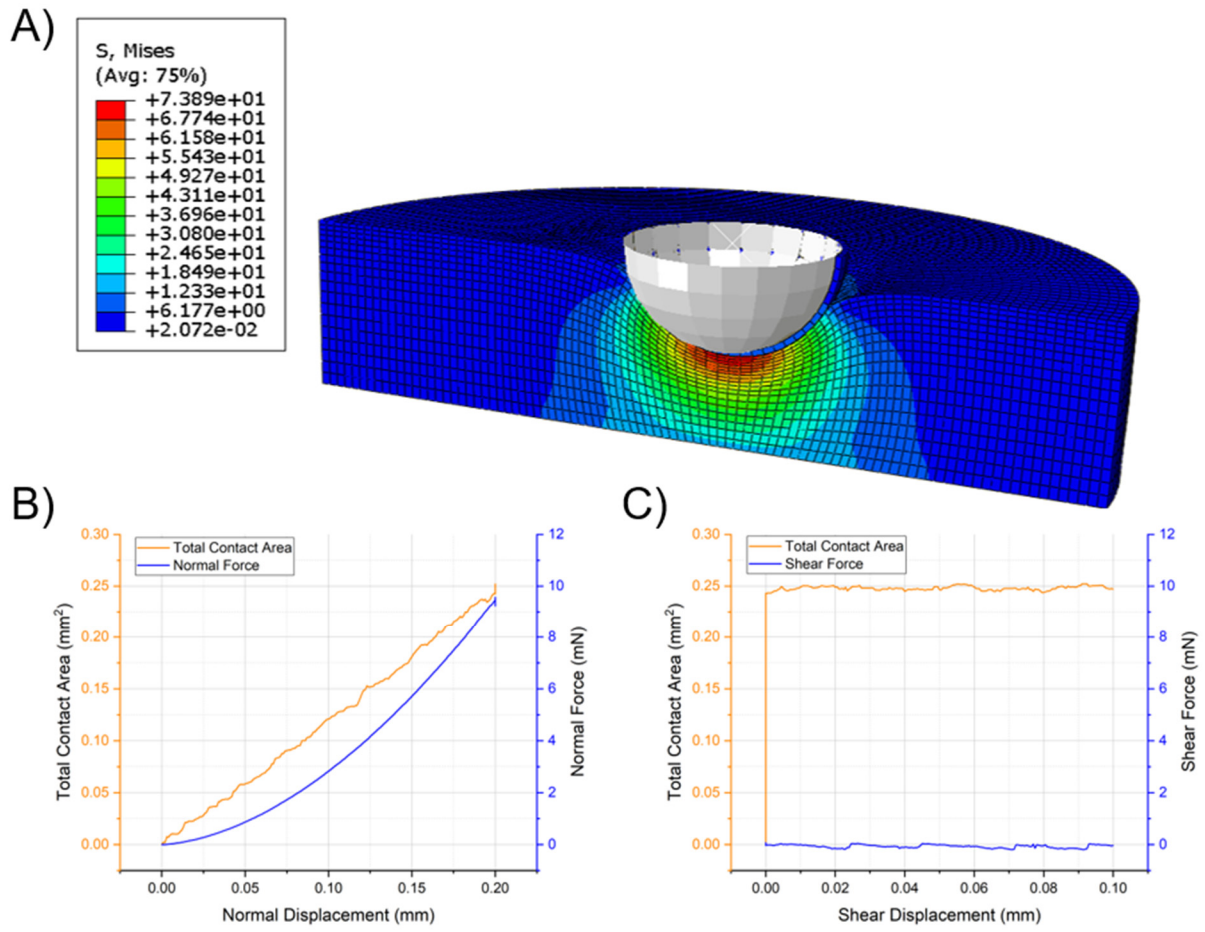

Figure S8: A) Post-processed stress field of the half space geometry used to simulate normal indentation and shear. B) Plot of the contact area and normal force versus normal displacement for the simulation. This plot shows that the normal force and contact area increase during normal loading as seen in experiments. C) Plot of the contact area and shear force versus shear displacement for the simulation. This plot shows that the contact area does not change during quasi static shear, as seen in experiments and the shear force stays roughly zero for an elastic material, which corresponds to our viscoelastic and poroelastic hydrogel after long relaxations periods, like those seen during imaging.

Refractive Index Mismatch Correction

The refractive index mismatch (RIM) correction factor presented in the paper was found by imaging a red florescent PDMS cylinder. The PDMS sample was imaged once through the hydrogel and once only through air. The pixel height of the hydrogel in each images stack is extracted and used to come up with a correction factor. Figure S9 shows the pixel height difference by showing half the fluorescent PDMS sample imaged through the gel and half the sample imaged through only air. The figure shows that the images acquired when RIM is present are distorted while the images acquired through air are representative of the actual size of the PDMS sample. An XY view is also shown of the samples to show the minimal distortion effects seen in the XY direction compared to the Z direction. Note these samples appear jagged around the edges in these images when compared to the other confocal image stacks shown in this paper. This can be attributed to the sample preparation method which required these samples to be cut from a flat sheet of PDMS rather than being molded or poured.

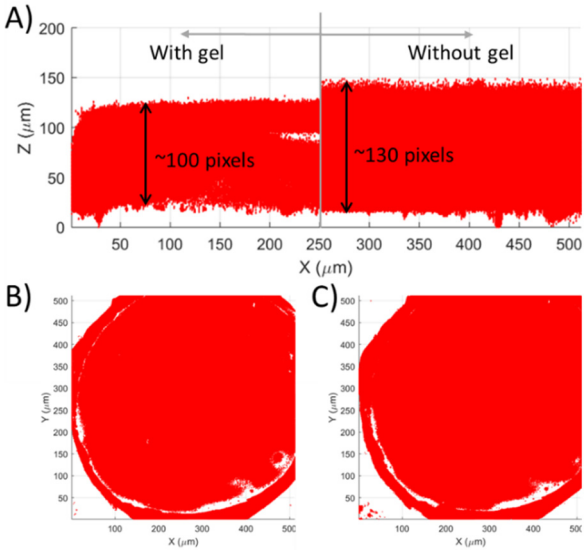

Figure S9: A) The two images of the PDMS sample stitched together to show the clear distortion cause by RIM in the z-direction. B) Shows the XY view of the sample imaged with through gel. C) Shows the XY view of the sample imaged through air only. In the XY plane minimal distortion is seen due to RIM and not XY correction is used.

Image Acquisition Time Study

The experimental method and data analysis techniques presented in this paper are used to reconstruct 3D contact interface surface profiles in near-equilibrium states. However, this method could also be utilized for investigating 3D contact interface surface profiles under shear sliding conditions. For reconstructing contact interface surfaces in transient states, much faster image acquisition times are necessary. An image acquisition study was done to investigate the relationship between image acquisition time and image resolution using various microscope settings. Figure S10A shows the results of this study and the resulting quality of the images using different microscope settings is shown in the representative images in Figure S10B. The nearest neighbor distance (NND) plots show that the contact interfaces are still identifiable with lower resolution image stacks and thus, this experimental method could be used to study contact interfaces in transient states like shear sliding (Figure S10C). Although these image stacks could be processed using the NND method, it should be noted that they are much lower resolution and therefore, could be more difficult to process depending on the interface parameters of interest.

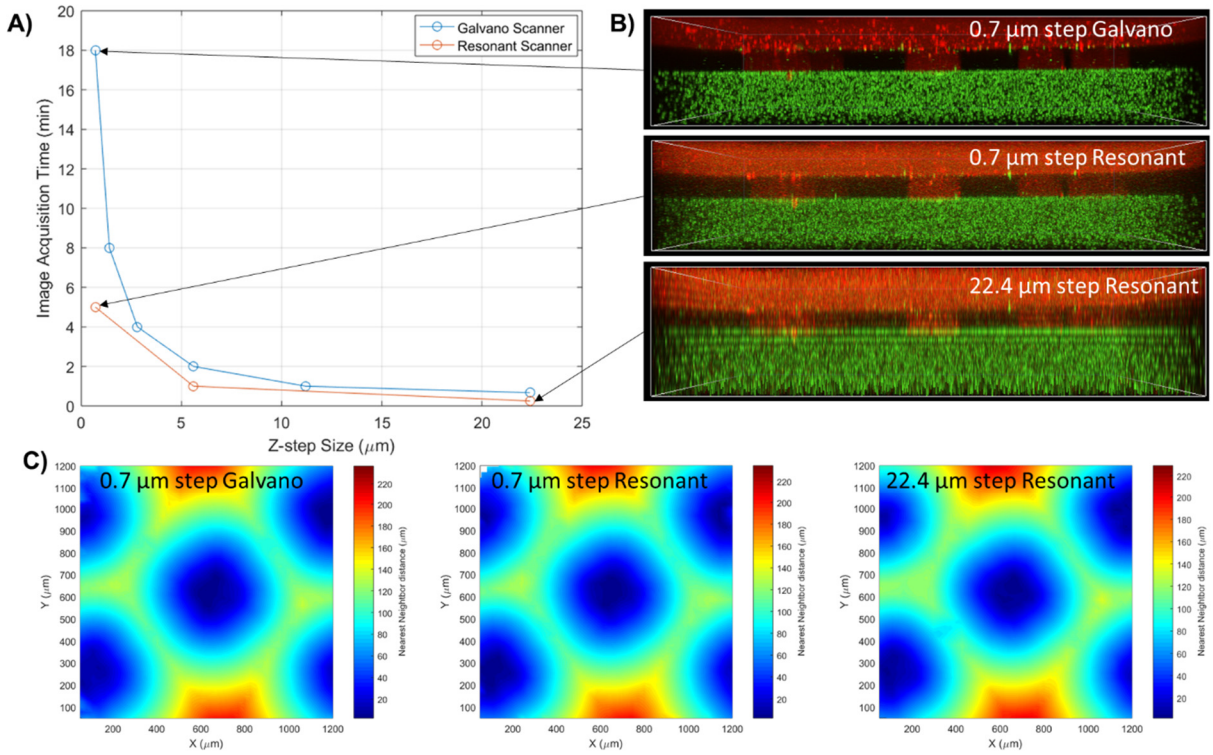

Figure S10: A) Image acquisition time as a function of z-step size for both galvano and resonant scanners. Each data point represents an image stack of 250 μm in height. B) Representative image stacks for 0.7 μm z-step size using galvano and resonant scanners as well as a 22.4 μm z-step size using the resonant scanner. A 0.7 μm z-step size was used for the data presented in the manuscript. C) NND plots for each of the representative image stacks shown in B. Note, while the NND plots look similar for these cases, other parameters such as surface geometry may be more difficult to analyze due to the lower resolution images.

Experimental Method Repeatability

The repeatability of this method was investigated by collecting an additional set of experimental data under the same normal indentation conditions as the data set shown in the Contact Area Under Normal Indentation section of the paper (represented by the pink markers in Figure S11). The only difference between these experiments is that during the second experiment, image stacks of the contact interface were only acquired every 50 μm of normal indentation, where the image data presented in the paper was acquired every 25 μm. From these two sets of data, we

concluded that the experimental method was repeatable.

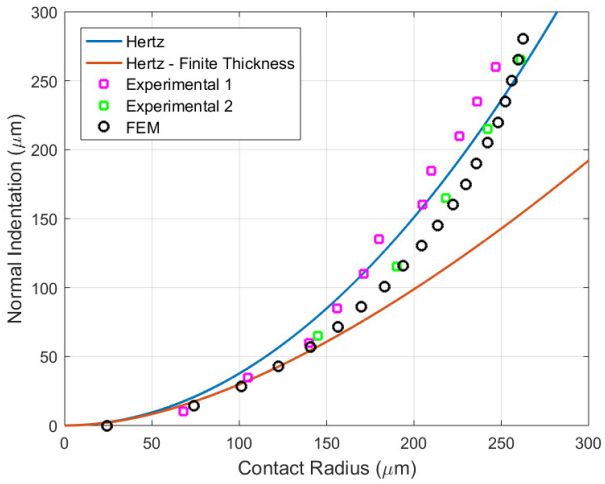

Figure S11: Data from the second experiment (green) is overlaid with the experimental data presented in the manuscript for Normal Indentation vs Contact Radius (Figure 3D). The agreement between these two experiments shows repeatability using this method.

Arbitrary Indenter Contact Area Identification

The NND method described in the paper can be used for identifying the contact between any fluorescently labeled arbitrary indenter geometry and a hydrogel with embedded particles. This method can be used with arbitrary geometries because the indenter and the substrate are both imaged at the interface and the method only relies on pixel intensity values for each within the image stacks rather than the indenter geometry itself. Figure S12A shows the results of the NND to analyze the contact interface between a hydrogel and an indenter with several flat punches of square cross-sectional geometry. These results demonstrate the utility of the NND method in identifying contact of an indenter with arbitrary geometry, more specifically, an indenter with non-circular contact as well as multiple unconnected contact regions in a single image stack. In addition, Figure S13 shows the reconstructed hydrogel surface with NND color map overlaid from the same indenter with several flat punches deeply indented into the gel substrate. Using the

NND method, we were able to identify the area of the indenter that is in contact with the gel substrate and how the contact area is distributed across the deformed surface profile of the hydrogel. This demonstrates the capability of our method to characterize the 3D contact between a soft gel substrate and an indenter with non-spherical geometry. It should be noted that the flat punch indenters are on a smaller scale than the spherical indenter used in the main text causing reconstructed surface noise to appear larger in comparison to the deformed surface from the larger spherical indenter.

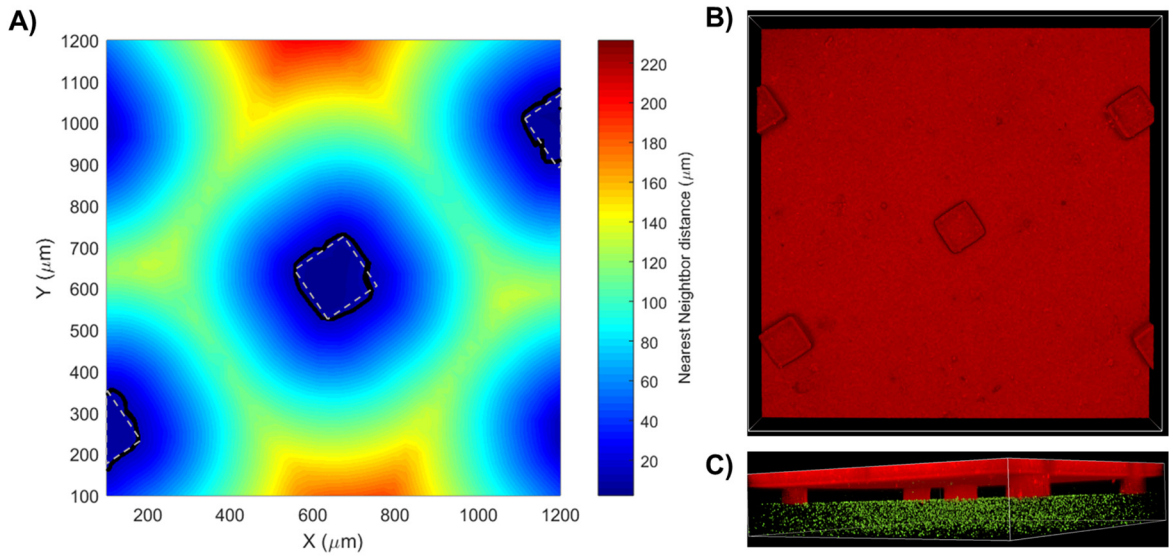

Figure S12: A) NND plot of contact between an indenter with several flat punches with square cross-sectional geometry and a hydrogel. The black solid line represents the contact identified by the NND and gray dashed line shows the known geometry of the indenter. Note that the nearest neighbor plot is cropped in comparison to the raw image in (B) and therefore, no contact region is identified for the two of the five flat punches. B) Bottom view of the fluorescent indenter (red) C) Isometric view showing both indenter (red) and hydrogel substrate (green particles).

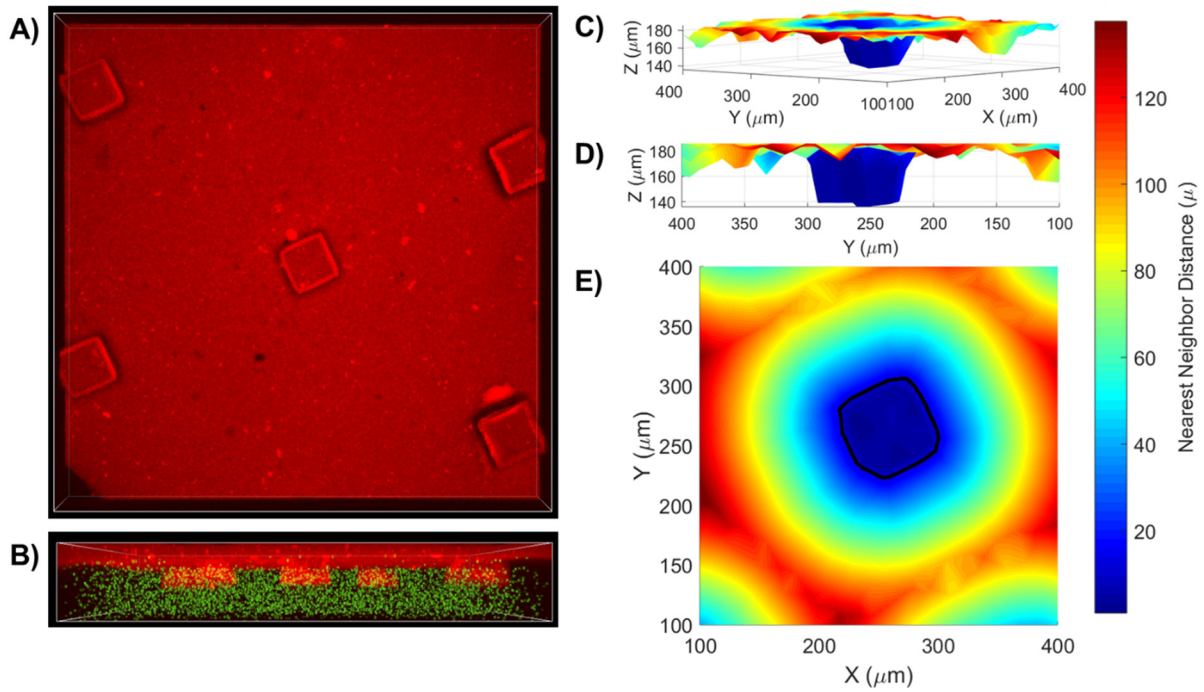

Figure S13: A) Bottom view of the fluorescent indenter (red) B) YZ view showing both indenter (red) and hydrogel substrate (green particles). C) Isometric view of the reconstructed gel surface with NND color map overlaid showing contact between the indenter and a hydrogel. Note that the NND surface reconstruction is cropped around the flat punch in the middle of the indenter in comparison to the raw image shown in (A) and (B). D) YZ view of the reconstructed gel surface with NND color map overlaid. E) Top view of the reconstructed gel surface with NND color map overlaid. The black solid line represents the contact boundary identified by the NND.

References

1. Fischer, R. S., Myers, K. A., Gardel, M. L. & Waterman, C. M. Stiffness-controlled three-dimensional extracellular matrices for high-resolution imaging of cell behavior. *Nat. Protoc.* **7**, 2056–2066 (2012).
2. Denisin, A. K. & Pruitt, B. L. Tuning the Range of Polyacrylamide Gel Stiffness for Mechanobiology Applications. *ACS Appl. Mater. Interfaces* **8**, 21893–21902 (2016).
3. Hu, Y., Chan, E. P., Vlassak, J. J. & Suo, Z. Poroelastic relaxation indentation of thin layers of gels. *J. Appl. Phys.* **110**, 86103 (2011).